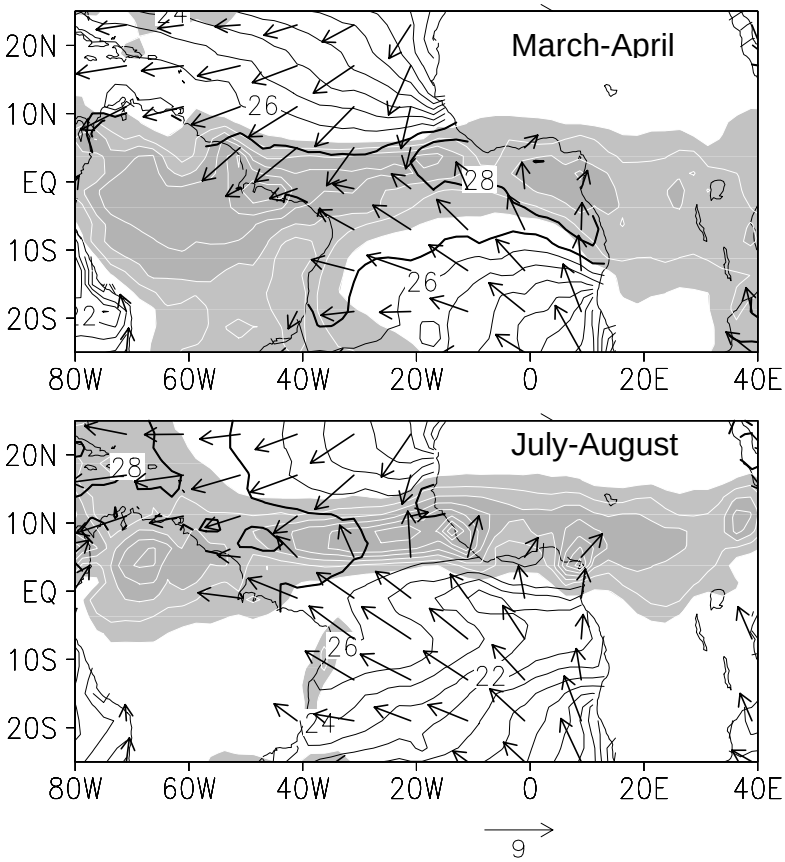

Fig. 1. Climatological distributions of rainfall (light shade > 2mm/day; dark shade > 6 mm/day), SST (contours in ^{o}C) and surface wind velocity (vectors in m/s) for March-April (upper) and July-August (lower panel), based on the Climate Prediction Center Merged Analysis of Precipitation (Xie and Arkin 1996) and Comprehensive Ocean-Atmospheric Data Set (Woodruff et al. 1987).

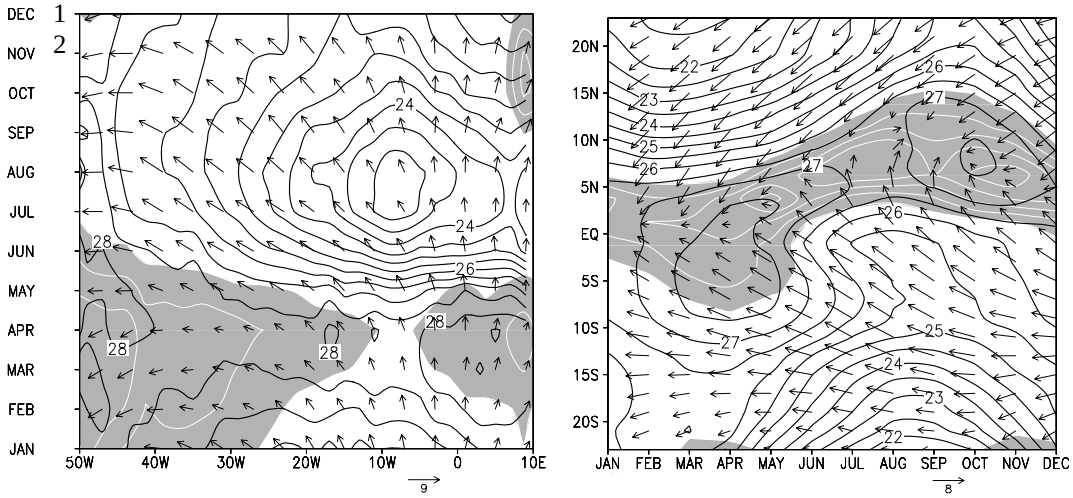

Fig. 2. Left: longitude-time sections of SST (black contours in ^{o}C) and surface wind velocity (vectors in m/s) at 1°S, and rainfall in 1.25^{o}S-1.25^{o}N. Right: time-latitude section of SST, surface wind velocity, and rainfall, averaged in 30-25°W. Rainfall are in white contours at 2.5 mm/day intervals with shade > 5 and 2.5 mm/day in the left and right panels, respectively.

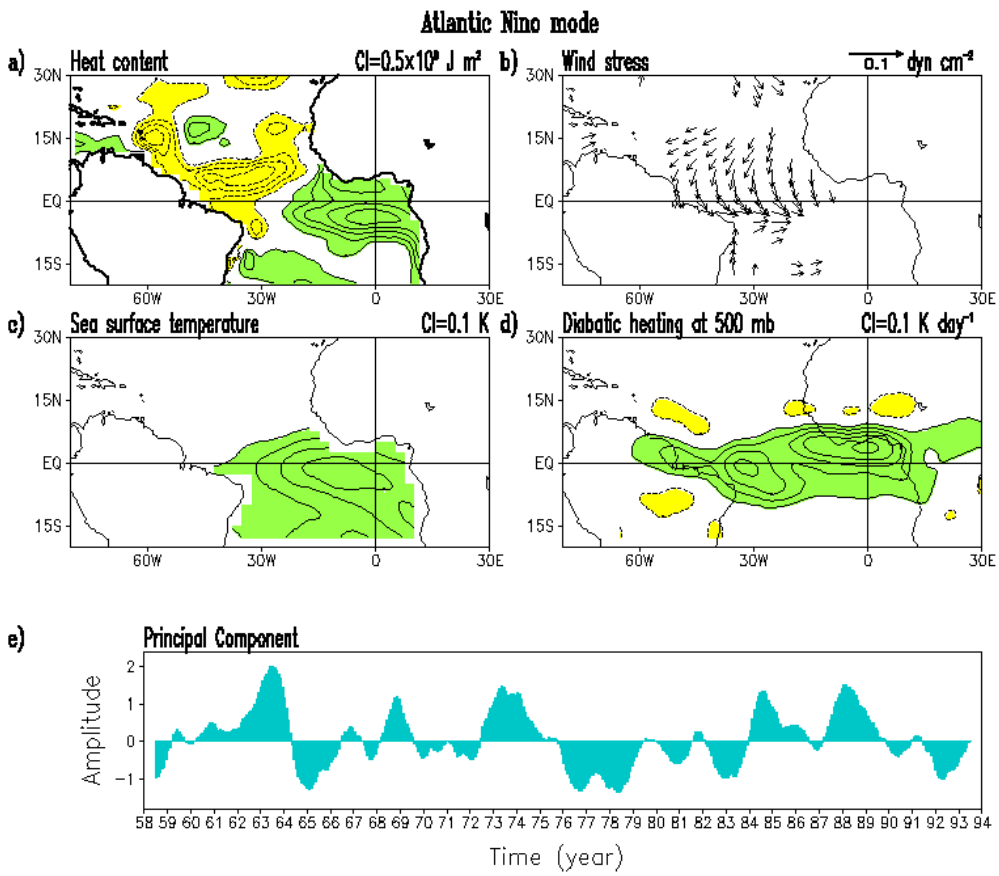

Fig. 3. Anomalies associated with the Atlantic Nino principal component from a five-component rotated principal component analysis of observed heat content ($\times 10^8\, Jm^2$, upper left), wind stress ($dyn\, cm^{-2}$, upper right), SST (^oC) middle left, diabatic heating at 500mb ($^oC\ dy^{-1}$, middle right) and the 12-month smoothed PC time series (bottom). From Ruiz-Barradas et al. (2000).

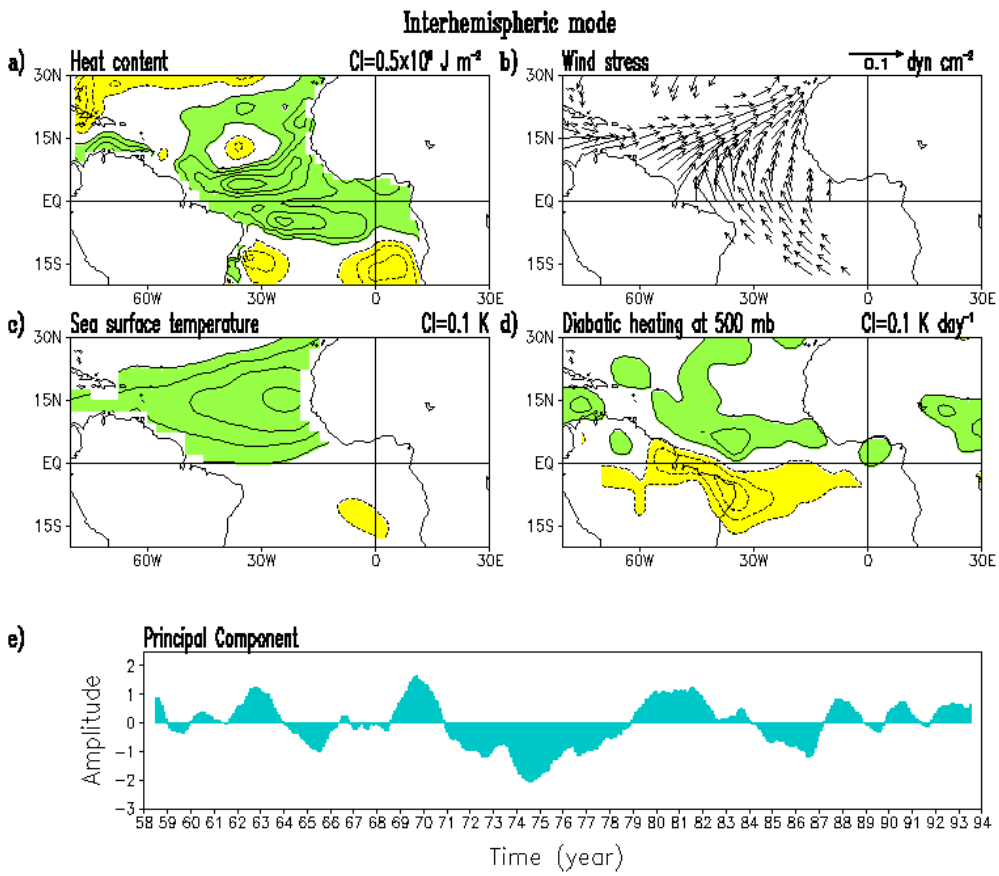

Fig. 4. Anomalies associated with the CESG principal component from a five-component rotated principal component analysis of observed heat content ($\times 10^8\, Jm^2$, upper left), wind stress ($dyn\, cm^{-2}$, upper right), SST (^oC) middle left, diabatic heating at 500mb ($^oC\ dy^{-1}$, middle right) and the 12-month smoothed PC time series (bottom). From Ruiz-Barradas et al. (2000).

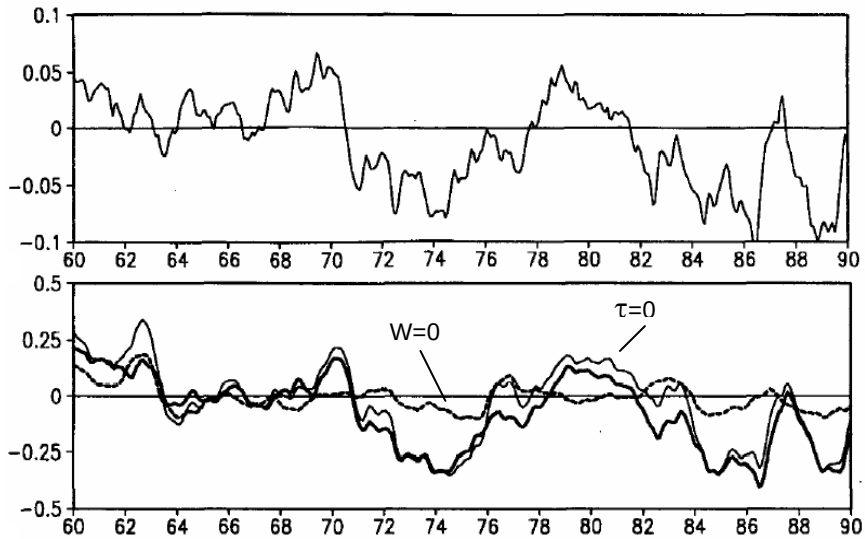

Fig. 5. Time series of 12-month smoothed interhemispheric differences in surface wind stress (upper panel in 10^{-1} Nm^{-2}) and SST (lower in ^{o}C). In the lower panel, results from the full simulation is in thick solid line, from runs removing wind variability in latent heat and momentum fluxes are in thin solid and dashed lines, respectively. From Carton et al. [1996].

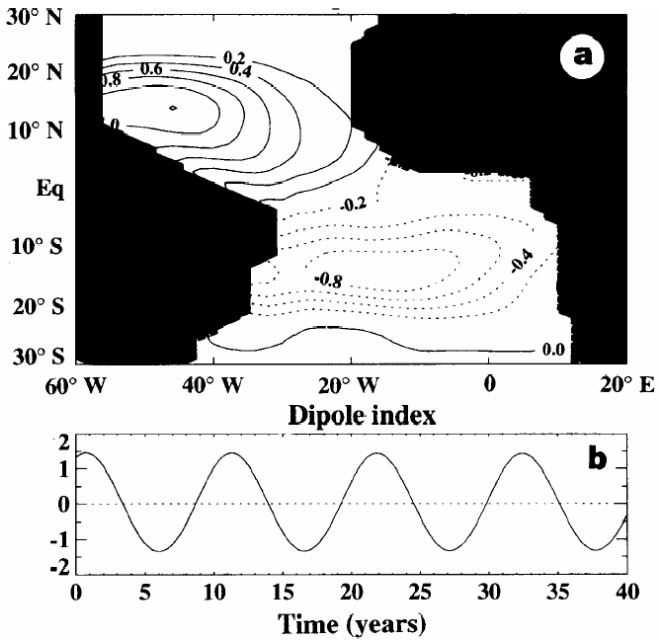

Fig. 6. SST regression (upper panel) against a CESG index (lower) in Chang et al.'s [1997] intermediate coupled model.

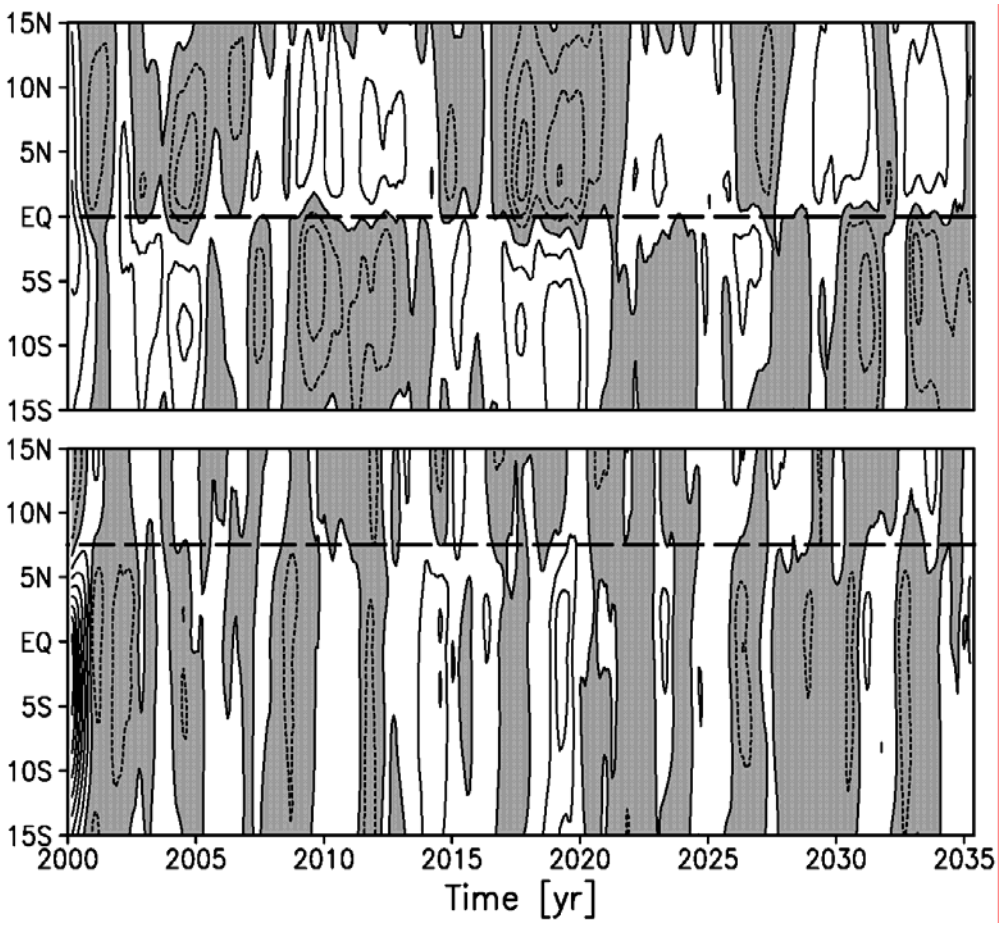

Figure 7. Time-latitude sections of zonal-mean SST anomaly (contours at 0.3^{o}C interval, with negative values shaded) in a coupled model. The thick dashed line indicates the latitude of the climatological ITCZ, which is symmetric about and displaced north of the equator in the upper and lower panels, respectively. From [*Okajima et al*., 2003].

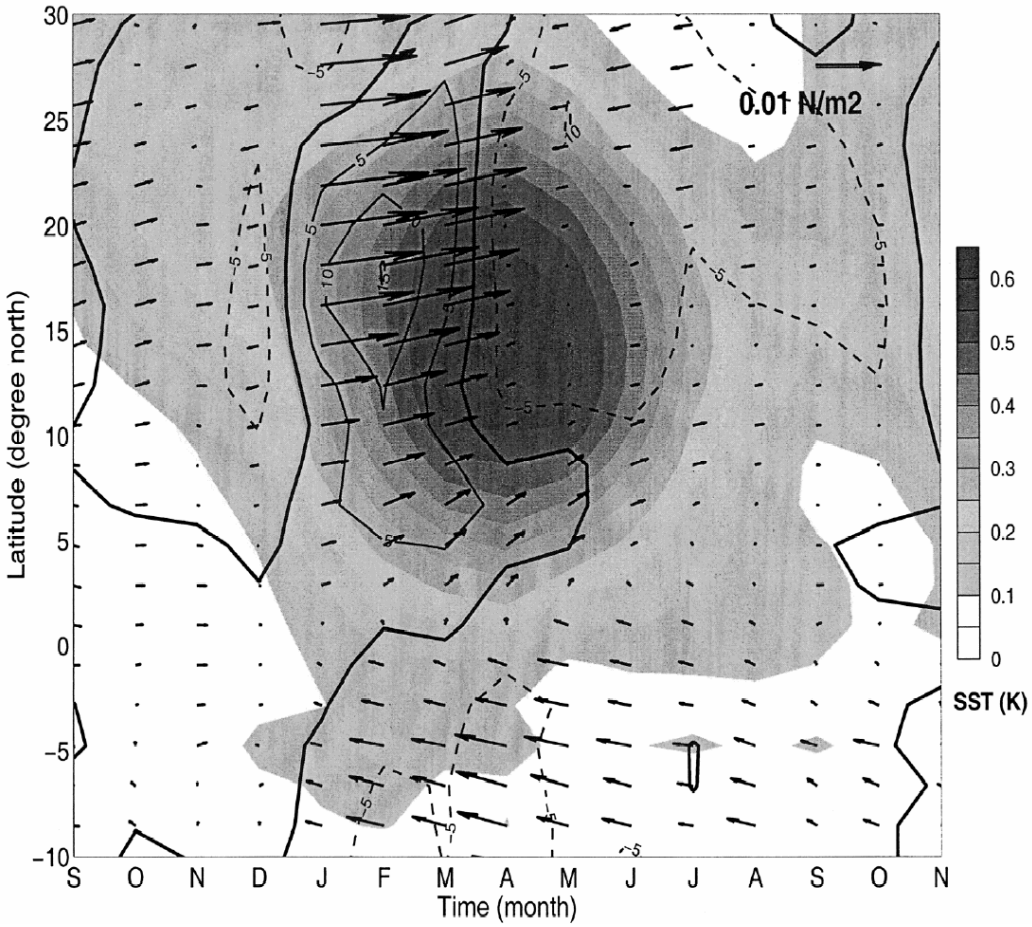

FIG. 8. Regression map of surface wind stress (arrows, scale in the top-right corner); net surface heat flux (contoured every 5 W m22, positive into the ocean, dashed when negative, zero contour thickened); and SST (shaded, in K) onto the NTA SST index time series in MAM. From Czaja et al. [2002].

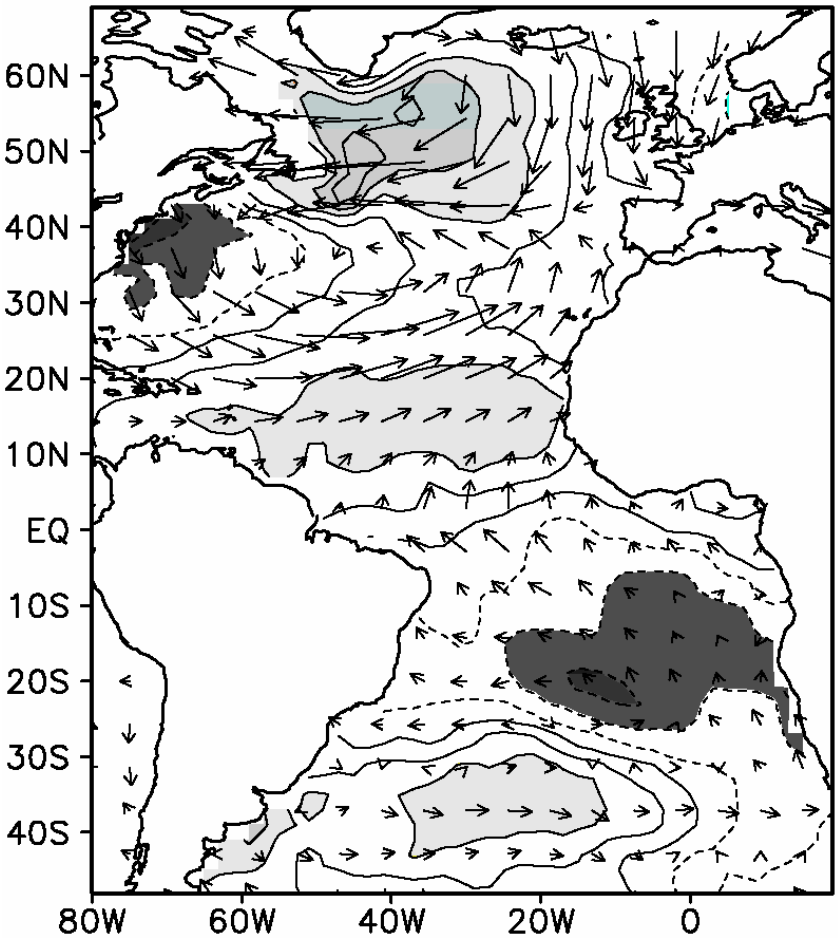

Fig. 9. Composite anomalies of SST and surface wind velocity in boreal winter based on a pan-Atlantic decadal oscillation index of Tanimoto and Xie [2002]. Global Sea Ice and SST dataset [*Parker et al*., 1994] and National Centers for Environmental Prediction Reanalysis [*Kalnay et al*., 1996] are used for SST and surface wind, respectively.

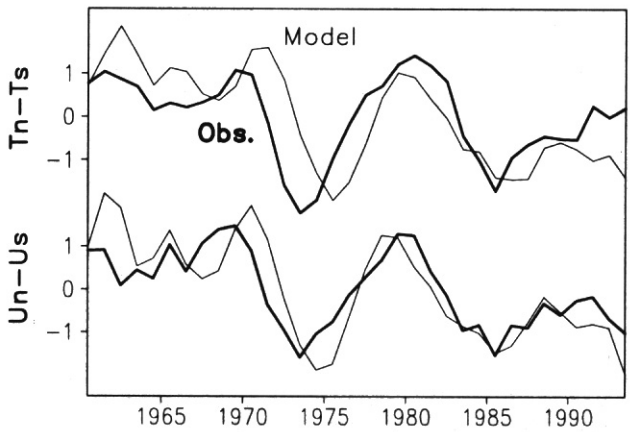

Fig. 10. Interhemispheric differences in SST and surface zonal wind velocity in COADS observations (thick) and simulated by a coupled model (thin). From Xie and Tanimoto [1998].

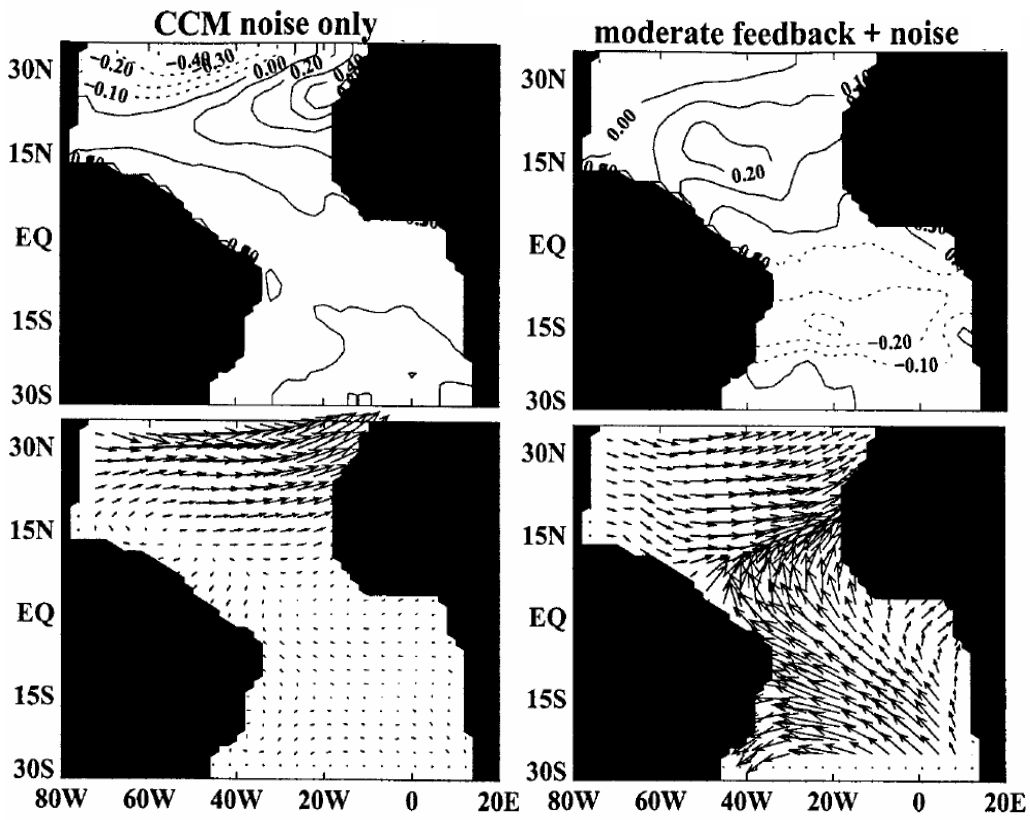

Fig. 11. The leading joint SVD modes of SST (upper panels), surface wind stress (lower panels), in coupled model runs forced by atmospheric noise, with (left panels) and without (right) feedbacks onto the atmosphere. From Chang et al. [2001].

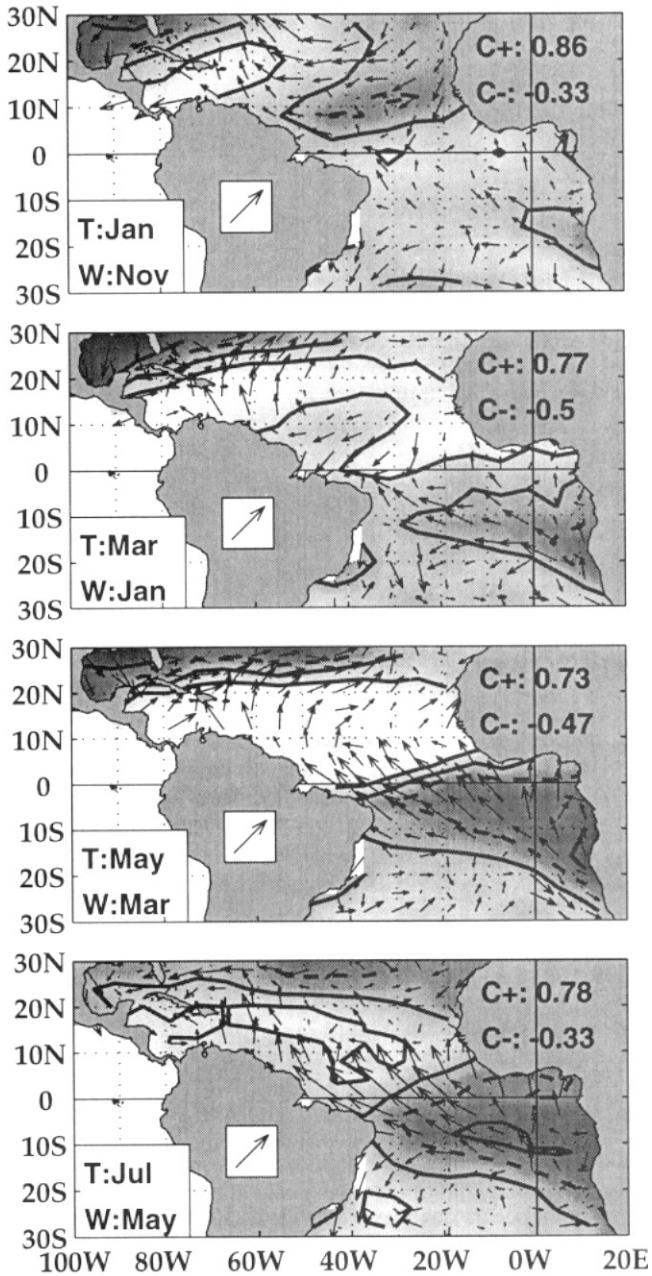

Fig. 12. Sequence of development of SST (T) and surface wind (W) correlations in the tropical Atlantic in response to ENSO. The zero contours are dashed, and negative values are dark shaded. From Enfield and Mayer [1997].

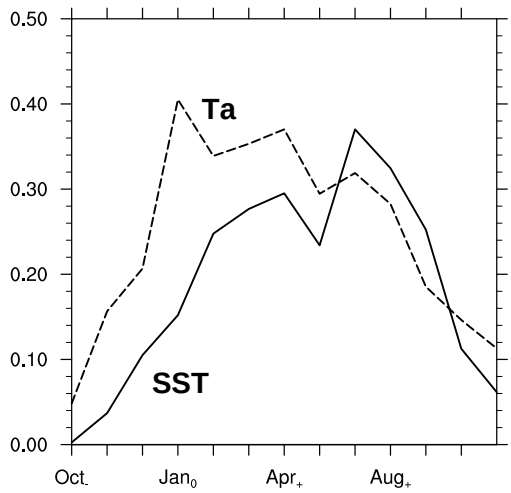

Fig. 13. Composite anomalies of COADS SST and surface air temperature averaged in the Caribbean Sea (80°W-60°W, 10°N-20°N), based on the November-January Nino3 index. From Chikamoto and Tanimoto [2004].